Analysis of the quality of crystallographic data and the limitations of structural models

Valentina Arkhipova, Albert Guskov, and Dirk-Jan Slotboom

Department of Biochemistry, Groningen Biomolecular Sciences and Biotechnology Institute, Zernike Institute for Advanced Materials, University of Groningen, Groningen, Netherlands

Crystal structures provide visual models of biological macromolecules, which are widely used to interpret data from functional studies and generate new mechanistic hypotheses. Because the quality of the collected x-ray diffraction data directly affects the reliability of the structural model, it is essential that the limitations of the models are carefully taken into account when making interpretations. Here we use the available crystal structures of members of the glutamate transporter family to illustrate the importance of inspecting the data that underlie the structural models. Crystal structures of glutamate transporters in multiple different conformations have been solved, but most structures were determined at relatively low resolution, with deposited models based on crystallographic data of moderate quality. We use these examples to demonstrate the extent to which mechanistic interpretations can be made safely.

Introduction

X-ray crystallography is an experimental technique that is used to determine three-dimensional structures of (biological) macromolecules crystallized in an orderly manner. As crystal structures provide visual models, which are typically used to interpret experimental data and generate new mechanistic hypotheses, it is essential that the limitations of crystal structures be carefully taken into account when making interpretations. The quality of the collected x-ray diffraction data are crucial for building a correct structural model. Without evaluation of the underlying crystallographic data, the use of deposited models could lead to erroneous conclusions of mechanistic features of the proteins.

Here we focus on the progress in crystallographic studies of the glutamate transporter family to illustrate to what extent mechanistic features can be reliably extracted from the crystallographic models. Glutamate transporters are an important family of secondary active transporters. In mammals, they play a crucial role in preventing neurotoxicity, by effecting reuptake of the neurotransmitter glutamate from the synaptic cleft. More than 20 structures of glutamate transporters in different conformational states have been determined, most of which have been obtained at medium resolution, producing models of rather moderate quality, with the inherent risk of over-interpretation. In this viewpoint, we inspect the crystallographic data and show that the use of the derived models could lead to erroneous conclusions of mechanistic features of the proteins. We underscore the importance of obtaining high-resolution and high-quality crystal structures for understanding the transport mechanism in detail.

Glutamate transporters

Glutamate transporters belong to a large family of secondary active transporters that catalyze uptake of acidic amino acids, neutral amino acids, or dicarboxylic acids in prokaryotes and eukaryotes (Slotboom et al., 1999; Vandenberg and Ryan, 2013; Grewer et al., 2014). Mammalian glutamate transporters, also called excitatory amino acid transporters (EAATs), play a key role in neuronal signaling by clearing excess neurotransmitter glutamate from the presynaptic cleft. EAATs couple glutamate uptake to symport of three sodium ions and one proton and to antiport of one potassium ion (Zerangue and Kavanaugh, 1996; Fig. 1). In Bacteria and Archaea, glutamate transporter homologues catalyze uptake of glutamate and aspartate as nutrients. These proteins are either proton- or sodium ion–dependent transporters and do not require potassium ions for transport (Tolner et al., 1995; Gaillard et al., 1996; Slotboom et al., 1999; Ryan et al., 2009).

Until recently, crystal structures were available only for glutamate transporter homologues from the Archaea *Pyrococcus horikoshii* (Glt_{Ph}) and *Thermococcus kodakarensis* (Glt_{Tk}; Table 1; Yernool et al., 2004; Boudker et al., 2007; Reyes et al., 2009, 2013; Verdon and Boudker, 2012; Jensen et al., 2013; Verdon et al., 2014; Akyuz et al., 2015; Guskov et al., 2016). Both Glt_{Ph} and Glt_{Tk} cotransport aspartate with three sodium ions and, in contrast to human EAATs, use neither proton nor potassium gradients (Boudker et al., 2007; Groeneveld

Correspondence to Albert Guskov: a.guskov@rug.nl; Dirk-Jan Slotboom: d.j.slotboom@rug.nl

Abbreviations used: EAAT, excitatory amino acid transporter; EPR, electron paramagnetic resonance; IFC, inward-facing conformation; iOFC, intermediate outward-facing conformation; OFC, outward-facing conformation; TBOA, D,L-threo-β-benzyloxyaspartate; TMS, transmembrane helical segment.
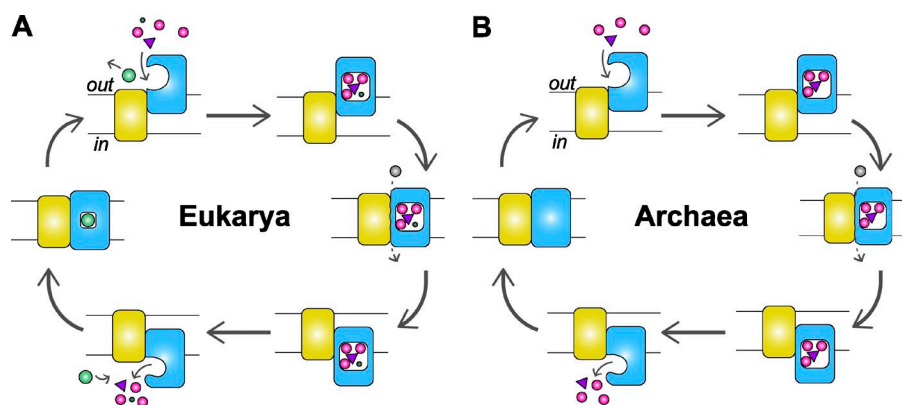
Figure 1. **Schematic representation of the glutamate transporter transport cycle.** (A) EAATs couple glutamate uptake to symport of three sodium ions and one proton and to antiport of one potassium ion. (B) The archaeal homologues Glt_{Tk} and Glt_{Ph} couple aspartate uptake only to symport of three sodium ions. Both mammalian and archaeal homologues were shown to support chloride conductance uncoupled to substrate transport. One protomer of the homotrimeric protein is depicted schematically in the membrane plane. The scaffold and transport domains are shown in yellow and blue, respectively; the position of membrane is indicated with the black lines, where "in" and "out" stand for inside and outside the cell, respectively. Sodium (magenta), proton (dark green), chloride (gray), and potassium (light green) ions are shown as circles, and substrate as a purple triangle. Possible chloride ion pathway is depicted with a dashed arrow.

and Slotboom, 2010; Guskov et al., 2016). Glt_{Ph} and Glt_{Tk} share high sequence identity with each other (77%) and with EAATs (~36%), with even higher conservation of amino acid residues involved in substrate binding (Boudker et al., 2007; Jensen et al., 2013; Silverstein et al., 2015). Structural studies of the archaeal Glt_{Ph} and Glt_{Tk} proteins have provided major insight into the transport mechanism of glutamate transporters. Recently, crystal structures of human EAAT1 have also been solved, revealing the architecture of the eukaryotic homologue (Canul-Tec et al., 2017).

Crystal structures overview

Glutamate transporters are homotrimeric proteins (Yernool et al., 2003, 2004; Gendreau et al., 2004; Canul-Tec et al., 2017), which had already been established for several family members before the first crystal structure was solved. Each subunit of the trimer has a complex topology of eight transmembrane helical segments (TMS1–8) and two helical hairpins (HP1 and HP2) that form two domains: a scaffold domain (TMS1, TMS2, TMS4abc, and TMS5), which is involved in trimerization, and a transport domain (TMS3, TMS6, HP1, TMS7ab, HP2, and TMS8), which contains the substrate and cation-binding sites (Fig. 2). Structural differences between the archaeal transporters and the human EAAT1 include deletions and insertions, as well as division of TMS1 into two and TMS8 into three separate helices, TMS1ab and TMS8abc, respectively.

Derivation of a mechanistic model of transport of the archaeal transporters has greatly benefited from crystal structures in different states, such as *apo*, substrate-bound, occluded binding site, and exposed binding site. Alternative access of the substrate-binding site to either side of the membrane is achieved via an elevator mechanism (for a review see Drew and Boudker, 2016; Ji et al., 2016; Ryan and Vandenberg, 2016), in which the transport domains move up and down relative to the trimerization domains, which are anchored in the membrane. The Glt_{Ph} transporter has been crystallized with the transport domain in the outward-facing conformation (OFC) and the inward-facing conformation (IFC), with the substrate-binding site located close to the extracellular or cytoplasmic space, respectively (Table 1 and Fig. 2, D and E; Yernool et al., 2004; Boudker et al., 2007; Reyes et al., 2009, 2013; Verdon and Boudker, 2012; Verdon et al., 2014; Akyuz et al., 2015). Comparison of the Glt_{Ph} structures in the OFC and IFC showed that both scaffold and transport domains are relatively rigid bodies that stay largely unchanged during the elevator-like movement (Reyes et al., 2009). Transfer of the transport domain is made possible by hinge movements in the short loops 2–3 and 5–6. As a result, the transport domain undergoes a transition of 16–18 Å toward the cytoplasm, accompanied by a rotation of ~37°.

Amino acid residues implicated in substrate and ion binding are highly conserved among glutamate transporters (Fig. 2 C; Boudker et al., 2007; Jensen et al., 2013). The substrate-binding site is formed by tips of HP1 and HP2, the unwound part of TMS7, and the central part of TMS8. In the OFC, helical hairpin HP2 occludes the bound substrate from the solvent in Glt_{Ph}, Glt_{Tk}, and EAAT1. The IFC structures of Glt_{Ph} showed a highly similar occluded conformation of the substrate-binding site. In this occluded state, the tips of structurally related HP1 and HP2 seal off the binding site.

Interpreting glutamate transporter structures | Arkhipova et al.

Table 1. **Summary of the available crystal structures of the glutamate transporter homologues**

Glt/EAAT1[a]	Ligand	Ions[b]	X-link	State	PDB ID	Resolution	Space group	Completeness[c]	Clash score[d]	R_{work}/R_{free}[e]	Comments, new features	Mutations	Reference
						Å		%		%			
Ph	Not assigned			OFC occluded	1XFH	3.5	P 6$_1$	97.1 (n.r.)	21	29.0/30.9	Homotrimer, bowl shape, overall fold	7H mutations: D37H, K40H, K125H, K192H, K223H, K264H, E368H	Yernool et al., 2004
Ph	L-Asp			OFC occluded	2NWL	2.96	P 6$_1$	69.3 (8.8)	5	23.6/26.5	Substrate-binding site	7H mutations	Boudker et al., 2007
Ph	L-Asp	Tl1, Tl2		OFC occluded	2NWX	3.29	P 6$_1$	69.2 (12.1)	15	26.3/28.6	Na1 and Na2 binding sites	7H mutations	Boudker et al., 2007
Ph	TBOA			OFC open	2NWW	3.2	P 6$_1$	74.8 (15.5)	8	24.1/26.0	Open conformation of HP2; *modeling of TBOA binding*	7H mutations	Boudker et al., 2007
Ph	L-Asp	Na1, Na2, Hg	HgCl$_2$	IFC occluded	3KBC	3.51	C 2 2 2$_1$	97.2 (84.5)	108	26.7/27.0	IFC, elevator mechanism	7H mutations, K55C, C321A, A364C	Reyes et al., 2009
Ph	L-Asp	Na1, Na2; Hg	HgCl$_2$	IFC occluded	3V8F	3.8	C 1 2 1	99.5 (97.6)	26	24.3/25.5	IFC, different mutant	7H mutations, V216C, C321A, M385C	Verdon and Boudker, 2012
Ph	L-Asp	Na1, Na2	HgCl$_2$	iOFC occluded	3V8G	4.66	C 1 2 1	73.1 (11.2)	14	25.5/29.4	*Intermediate OFC*	7H mutations, V198C, C321A, A380C	Verdon and Boudker, 2012
Ph	L-Asp	Na1, Na2; Hg	HgCl$_2$	OFC occluded	4IZM	4.5	P 6$_1$	99.7 (99.1)	12	25.0/29.9		7H mutations, L66C, S300C, C321A	Reyes et al., 2013
Tk				OFC occluded	4KY0	3.0	P 3$_2$ 2 1	99.8 (99.8)	13	21.2/26.6	OFC *apo protein without Na*	–	Jensen et al., 2013
Ph		Tl1, Tl2; Hg	HgCl$_2$	IFC occluded	4P6H	4.08	C 2 2 2$_1$	67.4 (6.4)	39	25.8/29.6	IFC *apo protein with Tl*	7H mutations, K55C, C321A, A364C, E418T	Verdon et al., 2014
Ph		*Tl/Ct*, Tl2; Hg	HgCl$_2$	IFC occluded	4P1A	3.75	C 2 2 2$_1$	99.7 (99.7)	24	23.0/25.7	*New cation site*	7H mutations, K55C, C321A, A364C	Verdon et al., 2014
Ph		Hg	HgCl$_2$	IFC occluded	4P19	3.25	C 2 2 2$_1$	99.1 (91.9)	23	22.2/25.8	IFC *apo protein without Na*	7H mutations, K55C, C321A, A364C	Verdon et al., 2014
Ph		Hg	HgCl$_2$	IFC occluded	4P3J	3.5	C 2 2 2$_1$	95.5 (93.2)	12	26.3/27.8		7H mutations, K55C, C321A, A364C	Verdon et al., 2014
Ph				OFC, occluded	4OYE	4.0	P 1 2$_1$ 1	70.3 (9.3)	13	24.9/26.6		7H mutations, R397A	Verdon et al., 2014
Ph	*Na1*			OFC occluded, tip open	4OYF	3.41	P 3$_1$	88.7 (12.2)	26	28.4/29.3	OFC *apo protein with Na*	7H mutations, R397A	Verdon et al., 2014
Ph	L-Asp	Na1, Na2		OFC occluded	4OYG/5CFY	3.5	P 3$_1$	97.1 (93.7)	24	24.9/29.4		7H mutations, R397A	Verdon et al., 2014
Ph	L-Asp	Na1, Na2		iIFC occluded	4X2S	4.21	P 6$_5$ 2 2	83.2 (18.3)	10	27.8/31.4	IFC occluded, *locked and unlocked*	7H mutations, R276S, C321A, M395R, E418T	Akyuz et al., 2015
Tk				OFC occluded	5DWY	2.7	P 3$_2$ 2 1	79.0 (17.9)	5	19.8/23.7	Improved 4KY0		Guskov et al., 2016
Tk	L-Asp	Na1, Na2, Na3		OFC occluded	5E9S	2.8	P 3$_2$ 2 1	97.4 (97.0)	8	21.3/24.3	Na3 site; loop 3–4; Na/L-Asp coupling mechanism		Guskov et al., 2016

Table 1. **Summary of the available crystal structures of the glutamate transporter homologues** (*Continued*)

Glt/EAAT1[a]	Ligand	Ions[b]	X-link	State	PDB ID	Resolution	Space group	Completeness[c]	Clash score[d]	R_{work}/R_{free}[e]	Comments, new features	Mutations	Reference
Hs	L-Asp, UCPH101	Na2		OFC occluded	5LLM	3.25	P 6_3	80.2 (39.1)	4	21.9/24.0	Glt_Ph-like fold, allosteric inhibition by UCPH101	73 mutations: R23S, Y44F, F46R, F50L, V51L, T56L, V60L, T62V, I63V, T67L, R72P, M73L, Y75P, S82A, Q93K, V96I, I101V, V105I, M108L, A110S, S113A, K118R, M119L, T129S, I137L, I141L, I143L, N155T, S175C, N204T, A223I, C232V, V236A, I237L, N239K, K241G, A246L, R248V, E249D, D252N, I258T, R260K, V264I, V271L, M287L, G288E, I290L, A295G, T298M, L306V, A309G, V310L, L316I, V320I, W326F, G330A, L332I, V336I, L388V, F399Y, N402D, S437A, F454L, L458F, T461M, T462V, S468A, H480K, K483E, N484K, R485Q, V487A, M489L	Canul-Tec et al., 2017
Hs	L-Asp, UCPH101	Na2		OFC occluded	5LM4	3.10	P 6_3	75.9 (31.7)	4	21.7/25.9	Nearly identical to 5LLM	73 mutations, K149A, M231I, F235I	Canul-Tec et al., 2017
Hs	L-Asp	Na2		OFC, occluded	5LLU	3.32	P 6_3	80.4 (40.1)	5	20.9/25.3	No inhibitors bound	73 mutations, M231I, F235I	Canul-Tec et al., 2017
Hs	UCPH101, TBOA_TFB			OFC open	5MJU	3.71	P 6_3	80.3 (40.5)	3	22.7/25.4	Similar to 5LLM but with HP2 tip open, **TBOATFB binding**	73 mutations	Canul-Tec et al., 2017

Indicators of low structure quality and uncertain features are shown in bold italic style.

[a]Ph, *Pyrococcus horikoshii* (Glt_Ph); Tk, *Thermococcus kodakarensis* (Glt_Tk); Hs, *Homo sapiens* (EAAT1).

[b]Na1, Na2, Na3, Tl1, Tl2, sodium or thallium ions included in the model in the corresponding sodium sites; Tl^{Ca}, thallium ion in the proposed cation-binding site.

[c]Overall completeness and completeness for the highest-resolution shell (in parentheses) as given in PDB data refinement statistics; n.r., not reported.

[d]Clash score value is given according to a global validation metrics of the PDB entry. It is calculated from the pairs of atoms in the model that are unusually close to each other (Chen et al., 2010) and expressed as a number of serious clashes (>0.4 Å) per thousand atoms. Values >20 are considered problematic.

[e]R_{free} is typically ~4–7% higher than R_{work}. The extremely small $R_{free} − R_{work}$ difference might indicate a compromised test data set (Wlodawer et al., 2008; Wlodawer, 2017).
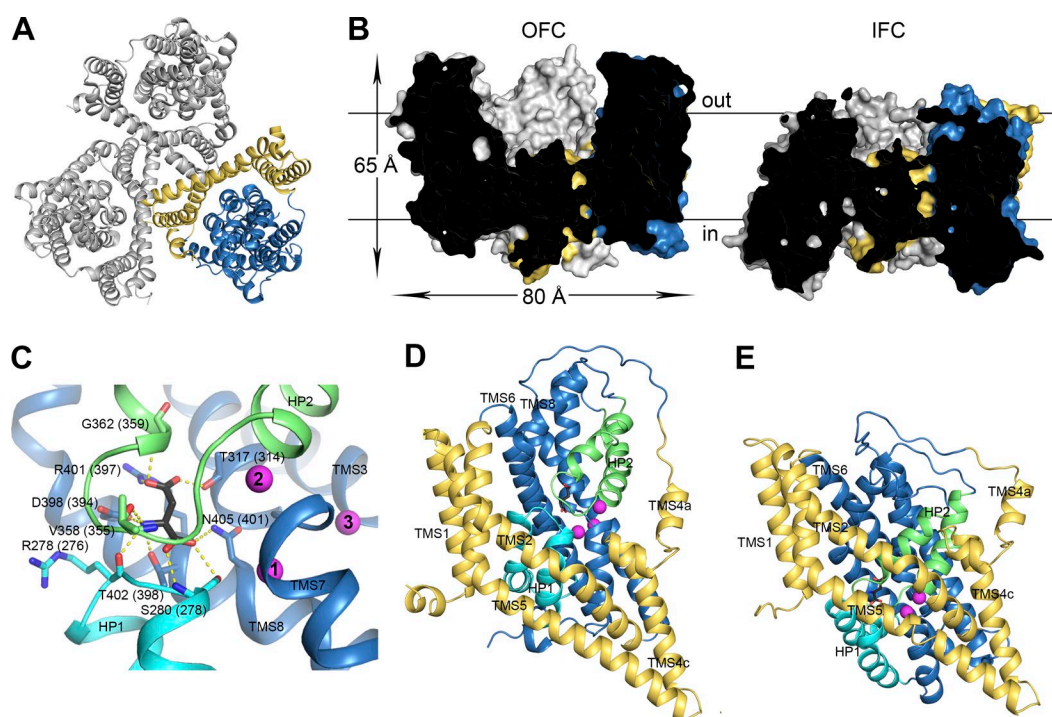
Figure 2. Structural architecture of the glutamate transporter homologues. (A) Extracellular view of the Glt$_{Tk}$ homotrimer; cartoon representation. The scaffold and transport domains of one of the protomers are shown in yellow and blue, respectively. (B) Cross-section of the Glt$_{Tk}$ trimer in the OFC (left) and Glt$_{Ph}$ in the IFC (right); protein in surface representation, the position of membrane indicated with the black lines. (C) Substrate-binding site in Glt$_{Tk}$ (residue numbering for Glt$_{Ph}$ in parentheses). L-Aspartate (black) and amino acid residues involved in substrate coordination are shown as sticks and sodium ions as purple spheres. HP1 and HP2 are shown in cyan and green, respectively. (D and E) Cartoon representation of protomers in OFC (D) and IFC (E). Color scheme as in A and C. PDB codes 5E9S and 3KBC, respectively.

Crystallization of Glt$_{Ph}$ in the OFC with the competitive inhibitor TBOA (D,L-threo-β-benzyloxyaspartate) revealed an open conformation of hairpin HP2, which had shifted ~10 Å in the direction of the 3–4 loop from its position in aspartate-bound Glt$_{Ph}$ (Boudker et al., 2007). The HP2 opening was explained by steric clashes with the benzyl group of the inhibitor modeled to the structure. Although this explanation is reasonable, it is important to note that the Glt$_{Ph}$-TBOA structure did not reveal electron density for the benzyl group of the inhibitor (see section TBOA binding and Fig. 6).

It was initially proposed for Glt$_{Ph}$ that HP2 would be mainly open in the *apo* state and that aspartate binding causes its closure. However, the first structure of the substrate-free transporter solved for the homologue Glt$_{Tk}$ revealed an OFC with occluded binding site and closed HP2 (Jensen et al., 2013). A structure of the substrate-free Glt$_{Ph}$ mutant R397A in OFC in the absence of sodium ions also showed an occluded conformation with HP2 in the closed state. The use of the R397A mutant was necessary to determine the structure of Glt$_{Ph}$ in *apo* form, because it has lower affinity for L-aspartate (6.6 µM vs. 27 nM for wild type; Verdon et al., 2014). The occluded *apo* state is probably required to reorient

the transport domain from the IFC to the OFC during the transport cycle.

The structure of Glt$_{Ph}$ mutant R397A crystallized in the presence of sodium, but absence of aspartate was similar to the structure of aspartate-bound Glt$_{Ph}$, except that the HP2 tip was slightly open (Verdon et al., 2014), with a proposed displacement of ~3 Å. However, the low resolution of the structure and absence of electron density for sodium ions (see section Cation-binding sites and Fig. 4) make it difficult to draw solid conclusions.

A structure of the Glt$_{Tk}$ homologue revealed the positions of all three sodium-binding sites (Guskov et al., 2016). The sites of two of the sodium ions (Na1 and Na2) correspond to the sites found earlier in the structure of Glt$_{Ph}$ crystallized with thallium ions (Boudker et al., 2007). The assignment of the third sodium ion allowed further insight into the mechanism of sodium and aspartate coupling during the transport (Guskov et al., 2016). It should be noted that the presence of a bound sodium ion usually cannot be established unequivocally based on the electron density alone because the number of electrons of a sodium ion is identical to that of a water molecule. Therefore, additional indicators such as geometry of the site, distances and angles, or alternative experiments are required for the assign-

ment. The Glt_{Tk} structures also allowed description of the long extracellular loop between TMS3 and TMS4 (Guskov et al., 2016) that plays an important role in the transport process (Compton et al., 2010). This loop was shown to cover the outer face of the transport domain in such a way that it might restrict movements of HP2 within the substrate-binding pocket.

Recent crystal structures of human EAAT1 provided the first insight into the structure of the eukaryotic glutamate transporters (Canul-Tec et al., 2017). EAAT1 was crystallized in the OFC in complex with ʟ-aspartate, and in the presence of allosteric and competitive inhibitors. The noncompetitive EAAT1-selective inhibitor $UCPH_{101}$ (2-amino-4-(4-methoxyphenyl)-7-(naphthalen-1-yl)-5-oxo-5,6,7,8-tetrahydro-4*H*-chromene-3-carbonitrile) was bound at the interface of transport and scaffold domains in a hydrophobic pocket between TMS3, TMS7, and TMS4c, more than 15 Å away from the substrate/sodium-binding pocket (Canul-Tec et al., 2017). Crystallization of EAAT1 with the TBOA derivative $TBOA_{TFB}$ (4-(trifluoromethyl)benzoylamino]benzyloxy]aspartate) showed a similar open conformation of HP2 as found in the Glt_{Ph}-TBOA model, but some care needs to be taken in interpretation of the electron density (see section TBOA binding).

Structural data quality indicators

The quality of crystal structures directly depends on the quality of the x-ray diffraction data that were used for their determination. Several articles and reviews describe valuable tools for evaluation of raw experimental data and solved macromolecular structures (Kleywegt, 2000; Wlodawer et al., 2008; Chen et al., 2010; Gore et al., 2012; Adams et al., 2016; Wlodawer, 2017).

Two general indicators for the quality of diffraction data are resolution and data completeness. Resolution defines the level of detail that can be seen in electron-density maps. Generally, resolutions of ~4 Å allow only backbone tracing and visualizing secondary structure elements (α-helices are often much better defined than β-strands). The assignment of side chains at low resolution is usually not possible, and the conformations of side chains in deposited models should be treated with caution. In structures solved at resolutions between 3 and 4 Å, the fold is typically described correctly, even though there is a considerable probability of erroneous assignments and wrong conformations of many side chains. Electron densities at 2.5–3-Å resolution usually allow for unambiguous assignment of the main chain and side chains for the rigid parts of a protein; however, in more flexible parts of a molecule, the probability of incorrectly placed side chains is still high. Ligands that fully occupy their binding sites usually are possible to visualize at this resolution, as well as highly ordered water molecules. At higher resolutions of 2–2.5 Å, auto-building procedures (Cowtan, 2006; Terwil-

liger et al., 2008) and experienced crystallographers are capable of building a (nearly) complete model and including most of the ordered solvent molecules and ligands in the correct conformations (Blow, 2002).

Most of the Glt_{Ph} structures were determined using crystals that diffracted to a moderate resolution of 3–4 Å (Table 1). Both structures of Glt_{Ph} with protomers containing transport domains in intermediate positions (Protein Data Bank [PDB] codes 3V8G and 4X2S), as well as Glt_{Ph} structures in OFC (4IZM and 4OYE) and IFC (4P6H), have resolution lower than or equal to 4 Å.

It is important to note that judging a crystal structure by resolution only is not good practice and could be misleading. Apart from the checking additional quality indicators (see below in this section), the electron-density maps should always be manually inspected. Often, moderate- and low-resolution structures provide electron-density maps of adequate quality to provide reliable insight in the general architecture, as well as some details of the macromolecule (still depending on the resolution). Conversely, models solved from data collected at high (atomic) resolution can have serious errors caused, for example, by insufficient completeness of data or inappropriate refinement protocols (Afonine et al., 2012).

Completeness of data can be defined by the number of collected crystallographic reflections in comparison to the number of theoretically possible reflections unique for the given crystal symmetry. For reliable refinement and model building, the overall completeness should be desirably higher than 90%, and values less than 80% (McRee, 1993) are considered poor. Because all reflections contribute to calculation of the electron-density map, the quality of maps calculated from incomplete data will be poor (Wlodawer et al., 2008). Table 1 shows structures that were solved from incomplete datasets (PDB codes 2NWL, 2NWX, 2NWW, 3V8G, 4P6H, 4OYE, 5DWY, and 5LM4).

Again, careful inspection of the electron-density maps is highly recommended to estimate the quality of the structural model. As an example, we compared the quality of the electron-density maps of two Glt_{Ph} structures in which the transport domain is in neither the OFC nor the IFC, but in an intermediate state (PDB codes 3V8G and 4X2S, with resolutions of 4.21 and 4.66 Å, respectively) with that of Glt_{Tk} (2.70-Å resolution). Fig. 3 shows electron densities for the highly conserved NMDGT motif, which is located in the unbound region of TMS7 and involved in formation of the substrate-binding and sodium ion–binding sites. The poor electron densities for both Glt_{Ph} structures in the intermediate states indicate a high chance of misinterpretation. Additionally, the low overall completeness (73.1% for the intermediate OFC) of the structural data affects the reliability of the model. It should be noted that the conclusion from these structures that the transport do-
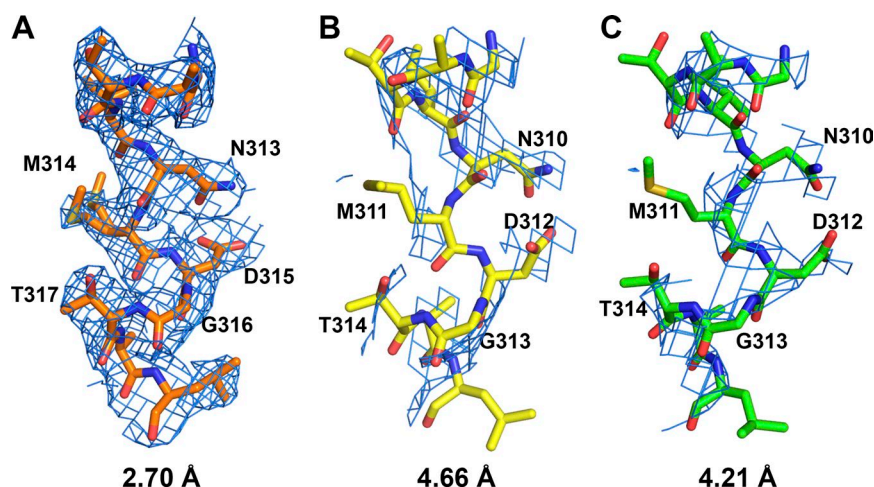
Figure 3. **Examples of electron densities for Glt_{Tk} and Glt_{Ph} structures.** (A–C) Representation of electron densities for the conserved NMDGT motif (shown as sticks) in the following structures: (A) Glt_{Tk} OFC (PDB code 5DWY); (B) Glt_{Ph} iOFC (PDB code 3V8G); and (C) Glt_{Ph} with asymmetric IFC protomers (PDB code 4X2S). The 2*Fo-Fc* electron-density maps (shown in blue mesh) are contoured at 1σ.

main is in an intermediate state is probably not affected by the data quality, but the details of the models should be treated with care.

The collected diffraction data (intensities of reflections) and the indirectly derived phases (see Glossary) are used to generate an electron-density map, which is used to build an initial protein model. Further crystallographic refinement includes multiple corrections of the model and improving phases to obtain the best agreement between the reflection amplitudes observed in experiment (*Fo*) and calculated from the model (*Fc*). This agreement is monitored with the so-called R-factor (or R_{work}), calculated as $\Sigma\ |Fo - Fc|/\Sigma Fo$. As cross-validation, an additional R-factor (R_{free}) is calculated using ∼5–10% of the reflections randomly chosen from the dataset and never included in the refinement process (Brünger, 1992). A low value of R_{free} is the most common indicator of successful refinement (the lower the value, the better the fit between the experimental data and the model). Comparing the values of R_{work} and R_{free} makes it possible to assess potential overfitting. There is a quasilinear relation between the difference between R_{free} and R_{work} resolution. $R_{free} - R_{work}$ differences for structures determined at 3–4-Å resolution should be ∼5%, and differences of less than 2% correspond to structures solved at resolution higher than 1 Å (Urzhumtsev et al., 2009).

The final structural model must conform to physical and chemical rules: the model must have reasonable crystal packing of molecules, contacts, and solvent content; correct stereochemistry; and correct bond lengths and angles. Furthermore, a model should have reasonable values for the crystallographic validation criteria: R-factors, B-factors (or displacement parameters which are commonly referred to as temperature factors), clash score (atomic overlaps), and Ramachandran outliers (torsion angles that fall into disallowed areas of a Ramachandran plot; Ramachandran et al., 1963), and it should have a best fit to an electron-density map.

Altogether, these parameters are used to analyze the structure quality. While analyzing structural statistics of glutamate transporter homologue structures, we observed that the PDB entries 1XFH, 2NWW, 3KBC, 3V8F, 4P3J, 4OYE, and 4OYF show a very small difference between R_{work} and R_{free} factors, which might indicate that the data that were set aside for R_{free} calculation were used at some stage of refinement (Wlodawer et al., 2008; Wlodawer, 2017), and thus could indicate possible overfitting.

Analysis and validation of structures
Appreciation of the limitations of these structural models will help prevent the generation of hypotheses and follow-up experiments for which there is no solid basis. Next, we discuss Glt_{Ph} structures in which sodium/potassium binding sites are interpreted (PDB codes 2NWX, 4P1A, and 4OYF), the TBOA-bound structure (PDB code 2NWW) and structures in which the transport domain is in neither the OFC nor the IFC, but in an intermediate state (PDB codes 3V8G and 4X2S; Table 1). The quality of the crystallographic data for these structures might have affected mechanistic interpretations.

Cation-binding sites. Difficulties in obtaining high-resolution Glt_{Ph} structures prevent visualization of sodium ions involved in transport. To model the positions of sodium-binding sites in Glt_{Ph}, thallium, which provides a strong anomalous signal, was used in crystallization experiments (Boudker et al., 2007; Verdon et al., 2014). This approach allowed for identification of the locations of sodium-binding sites Na1 and Na2, that were later observed in other crystal structures (Table 1), molecular simulations, and electrostatic calculation studies (Huang and Tajkhorshid, 2008; Gu et al., 2009; Holley and Kavanaugh, 2009; Larsson et al., 2010; Scopelliti et al., 2014), whereas for the Na2 site, other positions were also suggested (Gu et al., 2009; Heinzelmann and Kuyucak, 2014; Venkatesan et al., 2015).
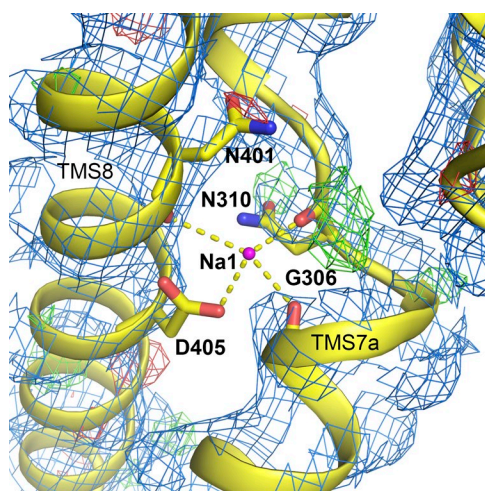
Figure 4. **Absence of electron density in the Na1 site for the** *apo* **Glt$_{Ph}$ structure (PDB code 4OYF).** The electron-density map (2*Fo-Fc*) is shown as a blue mesh and contoured at 1σ. The *Fo-Fc* map is colored in green (3σ) and red (−3σ). See Glossary for explanation of 2*Fo-Fc* and *Fo-Fc* maps. Cartoon representation; sodium ion Na1 assigned in this structure is shown as a purple sphere, and amino acid residues supposedly involved in its coordination are shown as sticks.

In the crystal structure of the Glt$_{Ph}$ mutant R397A (PDB code 4OYF), sodium ions were placed in the Na1 site. However, the absence of electron density in the map indicates that the sodium ion might have been placed incorrectly (Fig. 4). Moreover, in the substrate/sodium-binding site, the model does not fit properly in the density map. Assignment of water molecules at resolution 3.41 Å also seems inappropriate. In addition, the structural statistics of these data show an extremely small difference between R-factors (0.9%). All in all, the moderate data quality does not seem to provide a solid basis for the interesting suggestion that opening of the HP2 tip after sodium binding can be a mechanism preventing uncoupled uptake of sodium ions (Verdon et al., 2014). Furthermore, such a small movement of the HP2 loop (∼3 Å) in the medium-resolution structure could also be an over-interpretation, especially taking into account the significant coordinate error at this resolution.

Almost identical conformations of the Glt$_{Ph}$ OFC structures in the *apo* state and in the presence of sodium ions suggest minor conformational changes upon sodium binding to the *apo* protein. This result contrasts with electron paramagnetic resonance (EPR) and fluorescence data showing that sodium binding to the aspartate-free Glt$_{Ph}$ is followed by large conformational changes (Hänelt et al., 2013, 2015). Therefore, high-quality crystal structures of the transporter in the sodium-only state are needed to properly assess the conformation. The same applies for the Glt$_{Ph}$ structures in the IFC form in the presence of sodium ions, where the moderate resolution of 3.25–4.08 Å prevented visualiza-
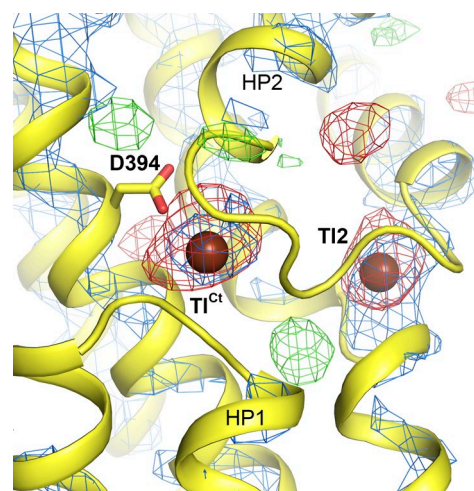

Figure 5. **Representation of the electron density for the thallium ions in the suggested cation-binding site (Tl^{Ct}) and Na2 site (Tl2) of Glt$_{Ph}$ (PDB code 4P1A).** The 2*Fo-Fc* map is colored in blue and contoured at 3σ. The *Fo-Fc* map is colored in green and red (±3σ). Difference maps are used to check the fit of the model to the diffraction data (see Glossary). The *Fo-Fc* difference map is a tool to visualize possible misfits and errors: positive peaks (green) indicate missing parts of the model, and negative peaks (red) indicate that these parts of the model are not supported by experimental data, and hence have to be removed. Additionally, negative density peaks might indicate inappropriate refinement of occupancies/B-factors and/or severe radiation damage. Cartoon representation; thallium ions are shown as brown spheres.

tion of relatively small conformational changes in the substrate-binding site.

Countertransport of a potassium ion is required for relocation of eukaryotic glutamate transporters to the outward-facing state. The position of the potassium-binding site was studied by mutational and computational studies (Kavanaugh et al., 1997; Zarbiv et al., 1998; Zhang et al., 1998; Bendahan et al., 2000; Rosental et al., 2006, 2011; Holley and Kavanaugh, 2009; Tao et al., 2010; Mwaura et al., 2012; Heinzelmann and Kuyucak, 2014), but the crystal structures of EAAT1 did not reveal potassium-binding sites (Canul-Tec et al., 2017). Although Glt$_{Ph}$ does not transport potassium ions (Raunser et al., 2006; Ryan et al., 2009), it was used for studies of countertransport because of structural similarity with EAATs. Soaking of the IFC *apo*-Glt$_{Ph}$ crystals with thallium ions revealed a new possible cation-binding site that overlaps with the aspartate-binding site (Verdon et al., 2014). Fig. 5 represents electron density in the suggested potassium-binding site (PDB code 4P1A, 3.75-Å resolution). For all three protomers, the difference map at 3σ shows negative density, indicating inappropriate refinement of occupancies or B-factors and/or severe radiation damage. It is possible that the mentioned cation-binding site is either an experimental artifact or a transition site of a sodium ion.

TBOA binding. TBOA is a competitive blocker of eukaryotic glutamate transporters (Shimamoto et al., 1998), and the structure of archaeal Glt$_{Ph}$ with TBOA revealed a movement of HP2 hairpin, providing a possible explanation of the inhibition mechanism (Boudker et al., 2007). Modeling of the inhibitor was based on the anomalous difference map calculated from diffraction data of the Glt$_{Ph}$ complex with 3-Br-TBOA, which reveals the position of the bromine atom. However, direct evidence based on electron density of the orientation of the full TBOA molecule in this structure is absent. Analysis of the Glt$_{Ph}$ TBOA structure (PDB code 2NWW) showed peaks of negative electron density for the bulky benzyl group of the inhibitor (Fig. 6). We calculated an electron-density omit map for the model and showed that the benzyl group of the blocker does not fit in the electron density. Instead, there might be an alternative possible orientation of the bound TBOA (Fig. 6) that could also cause displacement of HP2. Similar to Glt$_{Ph}$, an opening of HP2 was observed in the structure of human EAAT1 with TBOA$_{TFB}$ (PDB code 5MJU), where the position of the bound TBOA derivative also requires additional experimental confirmation.

Intermediate-state structures. We analyzed the electron densities of Glt$_{Ph}$ structures in intermediate states (PDB codes 3V8G and 4X2S). The structure of the Glt$_{Ph}$ V198C/A380C mutant showed an intermediate OFC (iOFC), where the transport domain of one of the protomers was shifted ~3.5 Å toward the cytoplasm and rotated ~15°, suggesting that during the inward movement, rotation of the transport domain precedes its inward translation (Verdon and Boudker, 2012). The structure of Glt$_{Ph}$ mutant R276S/M395R showed another asymmetric arrangement of protomers. The transport domain of one of the protomers was shifted 2 Å further inward and rotated by 7° (IFC locked configuration) in comparison with the original structure of Glt$_{Ph}$ in the IFC (mutant K55C/A364C), whereas the transport domains of the other two protomers moved from the scaffold domain by ~12° (IFC unlocked configuration) compared with the locked protomer (Akyuz et al., 2015).

The difficulties in obtaining crystal structures in intermediate states and the moderate quality of the available Glt$_{Ph}$ structures most likely are caused by high heterogeneity of the transporter conformations together with short lifetimes of the intermediates. The crystal lattice might be a factor that limits the number of observed conformations of the transporter. The presence of almost identical structures of Glt$_{Ph}$ for the two extreme states solved from crystals with different crystal packing (six space groups for outward-facing conformation P 1 2$_1$ 1, C 1 2 1, P 3$_1$, P 3$_2$ 2 1, P 6$_1$, and P 6$_3$ and two space groups for inward-facing conformation C 1 2 1 and C 2 2 2$_1$) gives credibility to the functional relevance of these
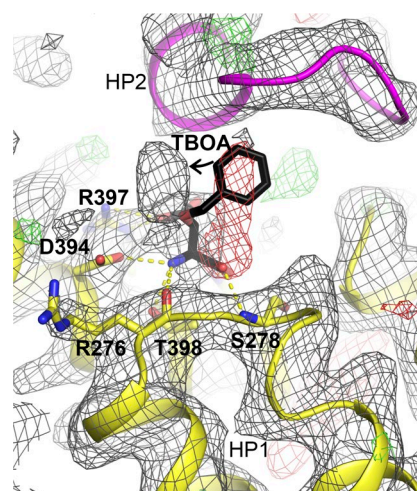

Figure 6. **Absence of electron density for the benzyl group of TBOA in the Glt$_{Ph}$ structure (PDB code 2NWW).** Possible alternative orientation of the benzyl group of TBOA (shown with an arrow). The electron-density omit map is shown in gray mesh (1σ). The *Fo-Fc* map is colored in green (3σ) and red (−3σ). Cartoon representation. HP2 loop is shown in purple. TBOA (shown in black) and residues involved in its binding are presented as sticks. Omit maps are used to remove bias (largely introduced by molecular replacement, where phases are taken from the similar structure, or caused by erroneous modeling) and can be used to verify assignment of ligands in binding sites. This is achieved by excluding a part of the model from the refinement procedure followed by the calculation of a bias-free difference map.

conformations. In addition, the existence of these states is consistent with a plethora of other data (Akyuz et al., 2013, 2015; Erkens et al., 2013; Georgieva et al., 2013; Hänelt et al., 2013; Ruan et al., 2017). However, the two structures of Glt$_{Ph}$ in different intermediate states (in space groups C 1 2 1 [iOFC] and P 6$_5$ 2 2 [IFC locked and unlocked protomers]) may be affected by crystal packing. The crystals of Glt$_{Ph}$ in the iOFC state (Verdon and Boudker, 2012) show contacts of the transport domain with symmetry molecules. Crystal contacts could also contribute to the stabilized (or forced formation) of the observed unlocked IFC state (PDB code 4X2S). The unlocked protomers (chains B and C) seem to have different crystal-packing environments than the single locked protomer (Fig. 7). Because of steric clashes between loop 4c-5 (chain B) and helix HP1b (chain C$_{sym}$) the 4c-5 hairpin is shifted in comparison with the locked chain. Therefore, the unlocked protomers from symmetry molecules could stabilize each other in the crystal lattice.

Conclusion and outlook

Intensive structural studies of glutamate transporter homologues have provided fundamental insight into protein architecture and transport mechanisms. Many interpretations of the determined structures are ex-
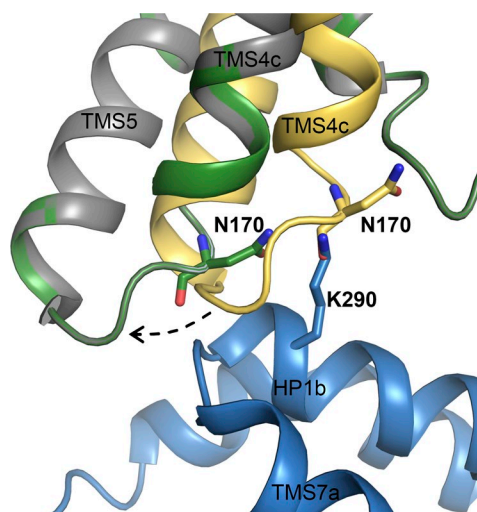
Figure 7. **Contacts between Glt_Ph asymmetric IFS protomers related by noncrystallographic symmetry (PDB code 4X2S).** Superposition of unlocked protomers B (green) and C (gray) and a locked protomer A (yellow). Chain C_sym of a symmetry molecule that forms an interface with chain B is shown in blue. Chains B and C_sym are symmetry mates, where steric clashes between the loop 4c-5 (chain B) and helix HP1b (chain C_sym) may have caused the shift of 4c-5 hairpin (shown with a dashed arrow), creating an "unlocked" conformation. Cartoon representation; amino acid residues that could cause steric clashes are shown as sticks.

tremely valuable and have greatly expanded our insight into membrane protein conformational changes. Nonetheless, some conclusions based on moderate-quality data might be over-interpretations.

The availability of similar crystal structures obtained for different crystallization conditions of different homologue proteins (Glt_Ph, Glt_Tk, EAAT1), with crystals of different space groups, as well as agreement with biophysical experiments (Akyuz et al., 2013, 2015; Erkens et al., 2013; Ruan et al., 2017), indicate the relevance of the OFC and IFC structural models. EPR studies showed that Glt_Ph is conformationally heterogeneous, in both detergent micelles and lipids (Georgieva et al., 2013; Hänelt et al., 2013). However, a high-resolution interpretation of the structural heterogeneity is lacking. Unfortunately, the moderate quality of Glt_Ph structures in intermediate states and potential crystal-packing effects diminish their usefulness.

The L-aspartate–binding site is well characterized in several Glt_Ph, Glt_Tk, and EAAT1 structures (Table 1), and the positions of all three sodium ions were found in the Glt_Tk OFC structure (Guskov et al., 2016). Lack of detailed structures hampers the determination of the position of sodium ions and subtle transitions in the substrate-binding site of IFC structures. Determination of high-quality structures of the proteins in the presence of sodium alone will be necessary to provide better insight into the sodium coupling mechanism.

Crystal structures with resolution of 2.5 Å or higher are necessary for unambiguous determination of positions of water molecules in the binding site, which is important for performing molecular simulations and understanding the influence of solvent on substrate/sodium coupling. Obtaining high-resolution structures of glutamate transporter homologues in different states and the combination of x-ray crystallography with molecular simulations and such techniques as single-molecule fluorescence resonance energy transfer (smFRET) and atomic force microscopy (AFM) should reveal gating events of transport cycle that still remain unclear.

The critical evaluation performed in this viewpoint is aimed to emphasize that care should be taken when using medium-quality structures as an input for further experiments, such as molecular dynamic simulations, EPR studies, and drug design. When using the structures of Glt_Ph in intermediate states, it is necessary to remember that crystal contacts could stabilize these conformations, and transport domains do not obligatorily pass these states while traversing the membrane. Similarly, metal cations that were placed in the deposited structural models solely on the basis that they theoretically should have been there, but for which experimental evidence such as electron density was lacking, should be treated with the utmost caution. The exact positions of the TBOA ligand and its derivative were not entirely determined based on electron density, which, for instance, will affect structure-based design of new inhibitors.

It is also important to realize that many of the solved crystal structures were not of the wild-type protein but of mutants that behaved better in expression, purification, and crystallization. The highest-resolution structures of the glutamate transporter homologues are reported for the Glt_Tk wild-type protein (Jensen et al., 2013; Guskov et al., 2016; although even in this case, the protein has an extra His-tag). Because crystallization of the wild-type Glt_Ph did not succeed, all Glt_Ph structures were obtained for the mutant proteins, with at least seven point substitutions of nonconserved amino acid residues. These mutants had a higher expression level and crystallized more successfully than the wild-type Glt_Ph (Yernool et al., 2004). Because of difficulties in purification of the wild-type EAAT1, thermostabilized versions of the protein were used for crystallization that share an overall sequence identity of ∼75% with the wild type and up to ∼90% identity at the substrate- and sodium-binding sites. In total, 73–76 mutations were introduced to increase protein stability and obtain functionally active protein (Canul-Tec et al., 2017). Although the function of the mutants appears to be largely unaffected compared with the wild-type protein, there may be yet-undetected functional differences.

Finally, as with any other structure deposited into the PDB database, one should remember that a structure is always a user interpretation of experimental data, and

it is prone to contain (some) errors. Therefore, the model should not be taken for granted, but the underlying data (including the electron-density map) should be explored and checked before planning new experiments to test hypotheses, or when using the models for explanations of biological functions.

Glossary

Reflections are defined as regularly spaced spots with varying intensities recorded on a detector as a result of x-rays scattering by a crystal. To generate an electron-density map, not only the amplitudes but also the phases are needed. **Phases** cannot be recorded during experiment, which is known as the **phase problem**. Phases can be obtained either via single (or multiple) isomorphous replacement (SIR/MIR), when a heavy atom is introduced into a crystal and then diffraction from a derivative crystal is compared with the one of a native crystal, and using direct methods to determine the positions of heavy atoms, which in turn helps to estimate phases; or by using anomalous x-ray scattering (single-wavelength anomalous diffraction [SAD] or multi-wavelength anomalous dispersion [MAD]) when an introduction of a heavy atom causes a phase shift (anomalous dispersion) used to estimate phases; or by using initial phases from a structurally similar protein (**molecular replacement**).

The **electron-density map** is the direct result of a crystallographic experiment and is a three-dimensional description of the electron density of the molecules in a crystal. A structural model of the molecules is built to fit the electron density.

After generating the initial electron-density map and building a starting model, structural **refinement** takes place, which aims to improve the phases and find the best agreement between the measured data and the constructed model.

Resolution (in crystallography) is a measure of details that can be distinguished in an electron-density map; measured in angstroms (1 Å = 0.1 nm).

Difference electron-density maps are used to check the fit of the model to the diffraction data. The **2Fo-Fc map** is a composite map that is commonly used as a working map against which the model is checked. The **Fo-Fc map** is a tool to visualize possible misfits and errors. **Omit maps** are used to minimize the model bias and are particularly useful to verify assignment of ligands in binding sites. Maps are typically countered at different levels of **sigma** (σ), which is referred to as the standard deviation. The typical sigma value for a 2Fo-Fc map is 1σ, and for a Fo-Fc map, 3σ.

R-factor, or R_{work}, is a measure of the agreement between the collected diffraction data and the model.

B-factor, or atomic displacement parameter (ADP), measures the displacement of an atom caused by thermal fluctuations, conformational disorder, and crystal lattice disorder. It is useful to detect the mobile portions of a model.

Occupancy of a given atom shows the fraction of molecules (from 0 to 1.00) in the crystal in which this particular atom actually occupies the position specified in the model.

REFERENCES

Adams, P.D., K. Aertgeerts, C. Bauer, J.A. Bell, H.M. Berman, T.N. Bhat, J.M. Blaney, E. Bolton, G. Bricogne, D. Brown, et al. 2016. Outcome of the first wwPDB/CCDC/D3R Ligand Validation Workshop. *Structure.* 24:502–508. https://doi.org/10.1016/j.str.2016.02.017

Afonine, P.V., R.W. Grosse-Kunstleve, N. Echols, J.J. Headd, N.W. Moriarty, M. Mustyakimov, T.C. Terwilliger, A. Urzhumtsev, P.H. Zwart, and P.D. Adams. 2012. Towards automated crystallographic structure refinement with phenix.refine. *Acta Crystallogr. D Biol. Crystallogr.* 68:352–367. https://doi.org/10.1107/S0907444912001308

Akyuz, N., R.B. Altman, S.C. Blanchard, and O. Boudker. 2013. Transport dynamics in a glutamate transporter homologue. *Nature.* 502:114–118. https://doi.org/10.1038/nature12265

Akyuz, N., E.R. Georgieva, Z. Zhou, S. Stolzenberg, M.A. Cuendet, G. Khelashvili, R.B. Altman, D.S. Terry, J.H. Freed, H. Weinstein, et al. 2015. Transport domain unlocking sets the uptake rate of an aspartate transporter. *Nature.* 518:68–73. https://doi.org/10.1038/nature14158

Bendahan, A., A. Armon, N. Madani, M.P. Kavanaugh, and B.I. Kanner. 2000. Arginine 447 plays a pivotal role in substrate interactions in a neuronal glutamate transporter. *J. Biol. Chem.* 275:37436–37442. https://doi.org/10.1074/jbc.M006536200

Blow, D.M. 2002. Outline of crystallography for biologists. Oxford University Press, Oxford. 248 pp.

Boudker, O., R.M. Ryan, D. Yernool, K. Shimamoto, and E. Gouaux. 2007. Coupling substrate and ion binding to extracellular gate of a sodium-dependent aspartate transporter. *Nature.* 445:387–393. https://doi.org/10.1038/nature05455

Brünger, A.T. 1992. Free R value: A novel statistical quantity for assessing the accuracy of crystal structures. *Nature.* 355:472–475. https://doi.org/10.1038/355472a0

Canul-Tec, J.C., R. Assal, E. Cirri, P. Legrand, S. Brier, J. Chamot-Rooke, and N. Reyes. 2017. Structure and allosteric inhibition of excitatory amino acid transporter 1. *Nature.* 544:446–451. https://doi.org/10.1038/nature22064

Chen, V.B., W.B. Arendall III, J.J. Headd, D.A. Keedy, R.M. Immormino, G.J. Kapral, L.W. Murray, J.S. Richardson, and D.C. Richardson. 2010. MolProbity: All-atom structure validation for macromolecular crystallography. *Acta Crystallogr. D Biol. Crystallogr.* 66:12–21. https://doi.org/10.1107/S0907444909042073

Compton, E.L.R., E.M. Taylor, and J.A. Mindell. 2010. The 3-4 loop of an archaeal glutamate transporter homolog experiences ligand-induced structural changes and is essential for transport.

Proc. Natl. Acad. Sci. USA. 107:12840–12845. https://doi.org/10 .1073/pnas.1003046107

Cowtan, K. 2006. The Buccaneer software for automated model building. 1. Tracing protein chains. *Acta Crystallogr. D Biol. Crystallogr.* 62:1002–1011. https://doi.org/10.1107/ S0907444906022116

Drew, D., and O. Boudker. 2016. Shared molecular mechanisms of membrane transporters. *Annu. Rev. Biochem.* 85:543–572. https ://doi.org/10.1146/annurev-biochem-060815-014520

Erkens, G.B., I. Hänelt, J.M.H. Goudsmits, D.J. Slotboom, and A.M. van Oijen. 2013. Unsynchronised subunit motion in single trimeric sodium-coupled aspartate transporters. *Nature.* 502:119– 123. https://doi.org/10.1038/nature12538

Gaillard, I., D.J. Slotboom, J. Knol, J.S. Lolkema, and W.N. Konings. 1996. Purification and reconstitution of the glutamate carrier GltT of the thermophilic bacterium Bacillus stearothermophilus. *Biochemistry.* 35:6150–6156. https://doi.org/10.1021/bi953005v

Gendreau, S., S. Voswinkel, D. Torres-Salazar, N. Lang, H. Heidtmann, S. Detro-Dassen, G. Schmalzing, P. Hidalgo, and C. Fahlke. 2004. A trimeric quaternary structure is conserved in bacterial and human glutamate transporters. *J. Biol. Chem.* 279:39505–39512. https://doi.org/10.1074/jbc.M408038200

Georgieva, E.R., P.P. Borbat, C. Ginter, J.H. Freed, and O. Boudker. 2013. Conformational ensemble of the sodium-coupled aspartate transporter. *Nat. Struct. Mol. Biol.* 20:215–221. https://doi.org/10 .1038/nsmb.2494

Gore, S., S. Velankar, and G.J. Kleywegt. 2012. Implementing an X-ray validation pipeline for the Protein Data Bank. *Acta Crystallogr. D Biol. Crystallogr.* 68:478–483. https://doi.org/10 .1107/S0907444911050359

Grewer, C., A. Gameiro, and T. Rauen. 2014. SLC1 glutamate transporters. *Pflugers Arch.* 466:3–24. https://doi.org/10.1007/ s00424-013-1397-7

Groeneveld, M., and D.J. Slotboom. 2010. Na(+):aspartate coupling stoichiometry in the glutamate transporter homologue Glt(Ph). *Biochemistry.* 49:3511–3513. https://doi.org/10.1021/bi100430s

Gu, Y., I.H. Shrivastava, S.G. Amara, and I. Bahar. 2009. Molecular simulations elucidate the substrate translocation pathway in a glutamate transporter. *Proc. Natl. Acad. Sci. USA.* 106:2589–2594. https://doi.org/10.1073/pnas.0812299106

Guskov, A., S. Jensen, I. Faustino, S.J. Marrink, and D.J. Slotboom. 2016. Coupled binding mechanism of three sodium ions and aspartate in the glutamate transporter homologue GltTk. *Nat. Commun.* 7:13420. https://doi.org/10.1038/ncomms13420

Hänelt, I., D. Wunnicke, E. Bordignon, H.-J. Steinhoff, and D.J. Slotboom. 2013. Conformational heterogeneity of the aspartate transporter Glt(Ph). *Nat. Struct. Mol. Biol.* 20:210–214. https:// doi.org/10.1038/nsmb.2471

Hänelt, I., S. Jensen, D. Wunnicke, and D.J. Slotboom. 2015. Low affinity and slow Na+ binding precedes high affinity aspartate binding in the secondary-active transporter GltPh. *J. Biol. Chem.* 290:15962–15972. https://doi.org/10.1074/jbc.M115.656876

Heinzelmann, G., and S. Kuyucak. 2014. Molecular dynamics simulations of the mammalian glutamate transporter EAAT3. *PLoS One.* 9:e92089. https://doi.org/10.1371/journal.pone .0092089

Holley, D.C., and M.P. Kavanaugh. 2009. Interactions of alkali cations with glutamate transporters. *Philos. Trans. R. Soc. Lond. B Biol. Sci.* 364:155–161. https://doi.org/10.1098/rstb.2008.0246

Huang, Z., and E. Tajkhorshid. 2008. Dynamics of the extracellular gate and ion-substrate coupling in the glutamate transporter. *Biophys. J.* 95:2292–2300. https://doi.org/10.1529/biophysj.108 .133421

Jensen, S., A. Guskov, S. Rempel, I. Hänelt, and D.J. Slotboom. 2013. Crystal structure of a substrate-free aspartate transporter. *Nat. Struct. Mol. Biol.* 20:1224–1226. https://doi.org/10.1038/ nsmb.2663

Ji, Y., V.L.G. Postis, Y. Wang, M. Bartlam, and A. Goldman. 2016. Transport mechanism of a glutamate transporter homologue GltPh. *Biochem. Soc. Trans.* 44:898–904. https://doi.org/10.1042 /BST20160055

Kavanaugh, M.P., A. Bendahan, N. Zerangue, Y. Zhang, and B.I. Kanner. 1997. Mutation of an amino acid residue influencing potassium coupling in the glutamate transporter GLT-1 induces obligate exchange. *J. Biol. Chem.* 272:1703–1708. https://doi.org /10.1074/jbc.272.3.1703

Kleywegt, G.J. 2000. Validation of protein crystal structures. *Acta Crystallogr. D Biol. Crystallogr.* 56:249–265. https://doi.org/10 .1107/S0907444999016364

Larsson, H.P., X. Wang, B. Lev, I. Baconguis, D.A. Caplan, N.P. Vyleta, H.P. Koch, A. Diez-Sampedro, and S.Y. Noskov. 2010. Evidence for a third sodium-binding site in glutamate transporters suggests an ion/substrate coupling model. *Proc. Natl. Acad. Sci. USA.* 107:13912–13917. https://doi.org/10.1073/pnas.1006289107

McRee, D.E. 1993. Practical protein crystallography. Second edition. Academic Press, San Diego. 477 pp.

Mwaura, J., Z. Tao, H. James, T. Albers, A. Schwartz, and C. Grewer. 2012. Protonation state of a conserved acidic amino acid involved in Na(+) binding to the glutamate transporter EAAC1. *ACS Chem. Neurosci.* 3:1073–1083. https://doi.org/10.1021/cn300163p

Ramachandran, G.N., C. Ramakrishnan, and V. Sasisekharan. 1963. Stereochemistry of polypeptide chain configurations. *J. Mol. Biol.* 7:95–99. https://doi.org/10.1016/S0022-2836(63)80023-6

Raunser, S., M. Appel, C. Ganea, U. Geldmacher-Kaufer, K. Fendler, and W. Kühlbrandt. 2006. Structure and function of prokaryotic glutamate transporters from Escherichia coli and Pyrococcus horikoshii. *Biochemistry.* 45:12796–12805. https://doi.org/10 .1021/bi061008+

Reyes, N., C. Ginter, and O. Boudker. 2009. Transport mechanism of a bacterial homologue of glutamate transporters. *Nature.* 462:880–885. https://doi.org/10.1038/nature08616

Reyes, N., S. Oh, and O. Boudker. 2013. Binding thermodynamics of a glutamate transporter homolog. *Nat. Struct. Mol. Biol.* 20:634– 640. https://doi.org/10.1038/nsmb.2548

Rosental, N., A. Bendahan, and B.I. Kanner. 2006. Multiple consequences of mutating two conserved β-bridge forming residues in the translocation cycle of a neuronal glutamate transporter. *J. Biol. Chem.* 281:27905–27915. https://doi.org/10 .1074/jbc.M600331200

Rosental, N., A. Gameiro, C. Grewer, and B.I. Kanner. 2011. A conserved aspartate residue located at the extracellular end of the binding pocket controls cation interactions in brain glutamate transporters. *J. Biol. Chem.* 286:41381–41390. https://doi.org/10 .1074/jbc.M111.291021

Ruan, Y., A. Miyagi, X. Wang, M. Chami, O. Boudker, and S. Scheuring. 2017. Direct visualization of glutamate transporter elevator mechanism by high-speed AFM. *Proc. Natl. Acad. Sci. USA.* 114:1584–1588. https://doi.org/10.1073/pnas.1616413114

Ryan, R.M., and R.J. Vandenberg. 2016. Elevating the alternating-access model. *Nat. Struct. Mol. Biol.* 23:187–189. https://doi.org /10.1038/nsmb.3179

Ryan, R.M., E.L.R. Compton, and J.A. Mindell. 2009. Functional characterization of a Na+-dependent aspartate transporter from Pyrococcus horikoshii. *J. Biol. Chem.* 284:17540–17548. https:// doi.org/10.1074/jbc.M109.005926

Scopelliti, A.J., G. Heinzelmann, S. Kuyucak, R.M. Ryan, and R.J. Vandenberg. 2014. Na+ interactions with the neutral amino acid transporter ASCT1. *J. Biol. Chem.* 289:17468–17479. https://doi .org/10.1074/jbc.M114.565242

Shimamoto, K., B. Lebrun, Y. Yasuda-Kamatani, M. Sakaitani, Y. Shigeri, N. Yumoto, and T. Nakajima. 1998. DL-threo-beta-benzyloxyaspartate, a potent blocker of excitatory amino acid transporters. *Mol. Pharmacol.* 53:195–201.

Silverstein, N., D. Ewers, L.R. Forrest, C. Fahlke, and B.I. Kanner. 2015. Molecular determinants of substrate specificity in sodium-coupled glutamate transporters. *J. Biol. Chem.* 290:28988–28996. https://doi.org/10.1074/jbc.M115.682666

Slotboom, D.J., W.N. Konings, and J.S. Lolkema. 1999. Structural features of the glutamate transporter family. *Microbiol. Mol. Biol. Rev.* 63:293–307.

Tao, Z., N. Rosental, B.I. Kanner, A. Gameiro, J. Mwaura, and C. Grewer. 2010. Mechanism of cation binding to the glutamate transporter EAAC1 probed with mutation of the conserved amino acid residue Thr101. *J. Biol. Chem.* 285:17725–17733. https://doi.org/10.1074/jbc.M110.121798

Terwilliger, T.C., R.W. Grosse-Kunstleve, P.V. Afonine, N.W. Moriarty, P.H. Zwart, L.-W. Hung, R.J. Read, and P.D. Adams. 2008. Iterative model building, structure refinement and density modification with the PHENIX AutoBuild wizard. *Acta Crystallogr. D Biol. Crystallogr.* 64:61–69. https://doi.org/10.1107/S090744490705024X

Tolner, B., T. Ubbink-Kok, B. Poolman, and W.N. Konings. 1995. Cation-selectivity of the L-glutamate transporters of Escherichia coli, Bacillus stearothermophilus and Bacillus caldotenax: Dependence on the environment in which the proteins are expressed. *Mol. Microbiol.* 18:123–133. https://doi.org/10.1111/j.1365-2958.1995.mmi_18010123.x

Urzhumtsev, A., P.V. Afonine, and P.D. Adams. 2009. On the use of logarithmic scales for analysis of diffraction data. *Acta Crystallogr. D Biol. Crystallogr.* 65:1283–1291. https://doi.org/10.1107/S0907444909039638

Vandenberg, R.J., and R.M. Ryan. 2013. Mechanisms of glutamate transport. *Physiol. Rev.* 93:1621–1657. https://doi.org/10.1152/physrev.00007.2013

Venkatesan, S., K. Saha, A. Sohail, W. Sandtner, M. Freissmuth, G.F. Ecker, H.H. Sitte, and T. Stockner. 2015. Refinement of the central steps of substrate transport by the aspartate transporter GltPh: Elucidating the role of the Na2 sodium binding site. *PLOS Comput. Biol.* 11:e1004551. https://doi.org/10.1371/journal.pcbi.1004551

Verdon, G., and O. Boudker. 2012. Crystal structure of an asymmetric trimer of a bacterial glutamate transporter homolog. *Nat. Struct. Mol. Biol.* 19:355–357. https://doi.org/10.1038/nsmb.2233

Verdon, G., S. Oh, R.N. Serio, and O. Boudker. 2014. Coupled ion binding and structural transitions along the transport cycle of glutamate transporters. *eLife.* 3:e02283. https://doi.org/10.7554/eLife.02283

Wlodawer, A. 2017. Stereochemistry and validation of macromolecular structures. *In* Protein Crystallography. Methods in Molecular Biology. A. Wlodawer, Z. Dauter, and M. Jaskolski, editors. Human Press, New York, NY. 595–610. https://doi.org/10.1007/978-1-4939-7000-1_24

Wlodawer, A., W. Minor, Z. Dauter, and M. Jaskolski. 2008. Protein crystallography for non-crystallographers, or how to get the best (but not more) from published macromolecular structures. *FEBS J.* 275:1–21. https://doi.org/10.1111/j.1742-4658.2007.06178.x

Yernool, D., O. Boudker, E. Folta-Stogniew, and E. Gouaux. 2003. Trimeric subunit stoichiometry of the glutamate transporters from Bacillus caldotenax and Bacillus stearothermophilus. *Biochemistry.* 42:12981–12988. https://doi.org/10.1021/bi030161q

Yernool, D., O. Boudker, Y. Jin, and E. Gouaux. 2004. Structure of a glutamate transporter homologue from Pyrococcus horikoshii. *Nature.* 431:811–818. https://doi.org/10.1038/nature03018

Zarbiv, R., M. Grunewald, M.P. Kavanaugh, and B.I. Kanner. 1998. Cysteine scanning of the surroundings of an alkali-ion binding site of the glutamate transporter GLT-1 reveals a conformationally sensitive residue. *J. Biol. Chem.* 273:14231–14237. https://doi.org/10.1074/jbc.273.23.14231

Zerangue, N., and M.P. Kavanaugh. 1996. Flux coupling in a neuronal glutamate transporter. *Nature.* 383:634–637. https://doi.org/10.1038/383634a0

Zhang, Y., A. Bendahan, R. Zarbiv, M.P. Kavanaugh, and B.I. Kanner. 1998. Molecular determinant of ion selectivity of a (Na+ + K+)-coupled rat brain glutamate transporter. *Proc. Natl. Acad. Sci. USA.* 95:751–755. https://doi.org/10.1073/pnas.95.2.751